Wavelength dependence of multiphoton ionization of xenon

Patrick Kaminski,[2,*] Rolf Wiehle,[2] Vincent Renard,[1] Anne Kazmierczak,[1] Bruno Lavorel,[1]
Olivier Faucher,[1] and Bernd Witzel[1,3,†]

[1]*Laboratoire de Physique de l'Université de Bourgogne, Dijon, Cedex, France*
[2]*Department of Molecular and Optical Physics, Albert-Ludwigs-Universität, 79104 Freiburg, Germany*
[3]*Département de Physique, Génie Physique et Optique, Université Laval, Pav Alexandre-Vachon, Québec, Canada G1K7P4*
(Received 12 July 2004; published 29 November 2004)

We have studied the multiphoton ionization of xenon atoms by 160 fs pulses at intensities of 5×10^{12} and 1.3×10^{13} W/cm^2 and present photoelectron kinetic energy and angular distribution spectra measured with a photoelectron imaging spectrometer. A noncollinear optical parametric amplifier allows us to tune the wavelength of the laser pulse over a range between 500 and 700 nm. Resonant and nonresonant processes as well as channel switching effects have been observed in this intensity and wavelength regime. Mainly resonant (5+1)-photon ionization via ns, nd, and nd' Rydberg states was studied in the region of 505–602 nm. Resonance structures were found related to the two fine structure ionization channels Xe$^+$ $^2P_{3/2}$ and Xe$^+$ $^2P_{1/2}$. In addition the (6+1)-photon resonant ionization and nonresonant 5- and 6-photon processes could be studied.

I. INTRODUCTION

The study of multiphoton ionization (MPI) processes, especially of noble gas atoms like xenon, for different laser intensities and wavelengths [1–6] has led to a significant advancement of our understanding of atomic dynamics in strong fields in the last decades. Aron and Johnson [7] discovered that the photoionization yield is resonantly enhanced when a laser excites intermediate states of xenon. Experiments made by Agostini *et al.* in 1979 [8] revealed that an electron can absorb additional photons after the ionization process in the so-called above-threshold ionization (ATI) process. In further experiments fine structure was found in the electron energy distribution and could be explained by transient resonances of ac Stark shifted Rydberg states [1,9]. The ionization of the heavier noble gases leads to two ionic ground states. In the case of the Xe$^+$ ion the two fine structure levels, $^2P_{3/2}$ and $^2P_{1/2}$, have an energy difference of 1.31 eV. Most studies of xenon in short pulse MPI experiments are focused on ionization into the $^2P_{3/2}$ channel and resonance enhancements due to excited states with a $5p^5$ $^2P_{3/2}$ ion core. Ionization into the $^2P_{1/2}$ channel was previously studied by Helm and Saeed [10] using 1 ps pulses, intensities of $(1-5) \times 10^{13}$ W/cm^2, and wavelengths between 308 to 344 nm. They observed four-photon ionization into both fine structure ionization channels. Bordas *et al.* [4] performed experiments at intensities of $(1-5) \times 10^9$ W/cm^2 with a nanosecond dye laser and observed three photon resonant four photon ionization of xenon. These authors observed that the final state distribution $^2P_{3/2}/^2P_{1/2}$ closely mirrors the core character of intermediate state resonances for nd and nd' states. However, they observed a suppression of the core character for ns and ns' intermediate states, which they identified as being due to the Cooper mini-

mum in the $ns \rightarrow \epsilon p$ transition. Also Rottke *et al.* [11] studied the intensity dependence of the photoelectron spectrum with 700 fs pulses and 526.5 nm wavelength. They observed ionization into the Xe$^+$ $^2P_{3/2}$ and $^2P_{1/2}$ fine structure states.

Only little work has been done in the wavelength range 500–650 nm and intensities between 10^{12} and 10^{13} W/cm^2 [11,12], where MPI is the dominant ionization mechanism. We cover this regime in our work and present photoelectron energy and angular spectra for wavelengths between 505 to 636 nm using 160 fs pulses. We made the measurements for two different pulse peak intensities: 5×10^{12} and 1.3×10^{13} W/cm^2. The combination of a photoelectron imaging spectrometer [13] and noncollinear optical parametric amplifier (NOPA) [14–16] systems allows us to measure the wavelength dependence of the MPI processes with the corresponding energy and angular distributions of the photoelectrons. The study of the frequency dependence of (5+1)- and (6+1)-photon resonant ionization allows an identification of the excited states involved in the ionization mechanism and enables a detailed insight into atomic dynamics in strong fields.

II. EXPERIMENTAL SETUP

We use a Ti-sapphire laser system (800 nm, 100 fs) with a chirped pulse amplifier to pump a homemade NOPA system delivering wavelengths between 500 to 700 nm at pulse energies from 10 to 30 μJ. A monochromator is used to determine the wavelength distribution within an accuracy of 0.35 nm. With a spherical mirror, the linear polarized beam is focused into the imaging spectrometer. The focal region represents a point source of photoelectrons. A static electric field (625 V/m) projects these electrons onto a multichannel plate (MCP) with a phosphor screen attached. The fluorescence of the phosphor screen caused by the impact of the electrons is recorded with a computer based CCD video camera. This picture gives us the possibility to extract the angular and energy distribution of the electrons. Typical experi-

---

*Electronic address: patrick.kaminski@pluto.uni-freiburg.de
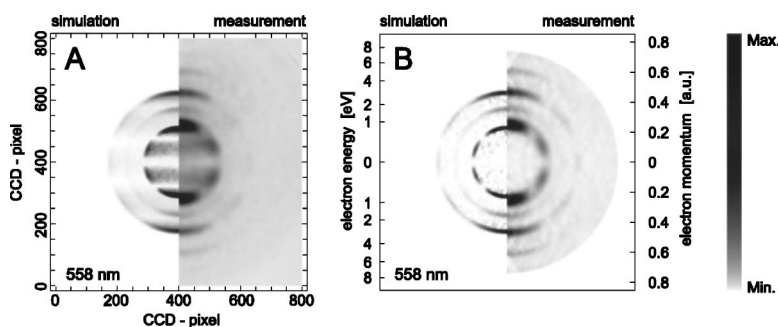†Electronic address: bernd.witzel@phy.ulaval.ca

FIG. 1. Comparison between simulation and experiment. (A) The raw photoelectron image. (B) The polar plot of the electron momentum distribution after Abel inversion of (A).

mental results are obtained by summing the electron signal from more than 300 000 single laser pulses. By changing the direction of the electric acceleration field the spectrometer is also suited to measure the time of flight spectrum of ions. The detection efficiency of the ion yield measurement is optimized with a higher electric acceleration field of 4500 V/m. For the laser intensities used in our experiments no doubly charged xenon ions were observed even at the maximum xenon partial pressure of 10^{-5} mbar. In order to avoid space charge effects, the electron distributions are recorded at partial pressures between 10^{-9}–10^{-8} mbar. The measured raw photoelectron images are Abelian transformed [17]. The statistic of the electron signal is optimized by a factor of 4 by a symmetrization routine. The polarization of the laser beam is parallel to the MCP detector and perpendicular to the static electric field. The distance of an observed photoelectron structure to the center of the phosphor screen depends linearly on its momentum perpendicular to the direction of the electric field. The well resolved ATI structure allows an accurate momentum calibration verified with a Monte Carlo simulation of the experiment.

III. ENERGY CALIBRATION OF THE IMAGING SPECTROMETER

The energy calibration of the electron imaging spectrometer is carried out in two ways. First, we compare a recorded electron spectrum at 558 nm with the result of a Monte Carlo simulation. Only the electron angular distribution and the ratio between both possible ionization channels $^2P_{1/2}$ and $^2P_{3/2}$ are used as an input from the experimental data. For the angular distribution we use the fit parameters obtained in least-square fits from an expansion in Legendre polynomials (see Sec. VI). All other experimental parameters, e.g., the detection system, the spectral bandwidth of the laser, the position of the laser focus in respect to the detector as well as the static electric field, are included in this simulation. The number of electrons used in the simulation is comparable to the number of electrons detected in the experiment. We assume a population of the 6*d* Rydberg state during the ionization process and neglect any laser induced ac Stark shift. Figure 1(A) shows a simulated raw photoelectron image on the left half and the experimentally observed image on the right half. We include the digitalization function of the CCD camera, allowing us to present both images in units of pixel. Figure 1(B) is a comparison between the experimental result and the corresponding simulation after the Abelian deconvo-

lution procedure. Each observed concentric ring in Fig. 1 belongs to a group of electrons with the same value of momentum and can be assigned to an ionization channel related to the population of a resonant intermediate Rydberg state. Additional rings appear in the images because of above-threshold ionization. The distance between the ATI peaks corresponds to 2.2 eV, the energy of one photon at 558 nm. Due to the fine structure splitting of the ionic ground state, we observe two different ATI series. These series are separated by 1.31 eV the energetic difference between the $^2P_{1/2}$ and $^2P_{3/2}$ fine structure states. The width of the experimental electron distribution appears wider because the Monte Carlo simulation assumes resonant population of a single 6*d* Rydberg state only. The good agreement between experiment and simulation allows us an absolute calibration of the momentum scale. This calibration is verified by the measurement of the energy difference of electrons originating from different ATI processes. The difference in kinetic energy of the ATI orders of a MPI process is given by the photon energy, i.e., 2.46 eV for 505 nm, 1.95 eV for 636 nm and the radius of the rings is proportional to the square root of the kinetic energy of the electrons. Both techniques are used to identify the resonant states shown in Figs. 5 and 6.

IV. RESULTS

Electron momentum distribution spectra are recorded for laser wavelengths in the region of 505 to 636 nm. First we want to give an overview of the observed processes. A detailed discussion of the different ionization channels is given in the next section. The structure appearing in the transformed photoelectron images (cf. Figs. 2 and 3) can be understood by resonant or nonresonant MPI processes. For the verification of these two ionization paths in the observed electron momentum distributions, the intensity distribution at the laser focus must be taken into account.

A. Resonant ionization

Excited intermediate states as well as the ionization threshold are pondermotively shifted by the electric field of the laser pulse. At the very low laser intensities used in this experiment, the shift is small compared to the energy of a single photon. In the case of a resonant $(n+1)$-photon ionization process the kinetic energy of the observed electron is given by
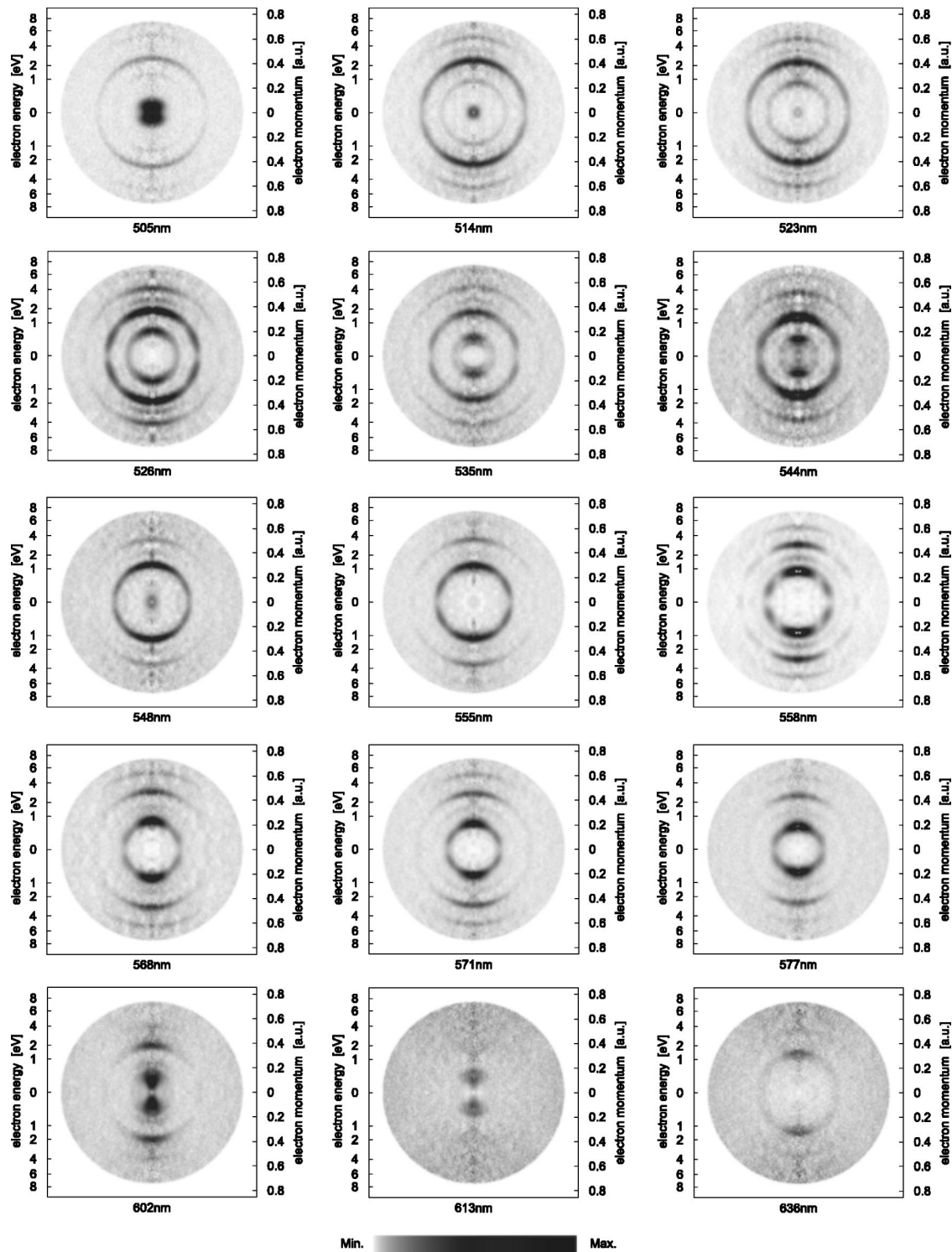
FIG. 2. Polar plots of the electron momentum distribution recorded at various wavelengths and an intensity of 5×10^{12} W/cm^2. The laser polarization is directed along the vertical axis of the figure. The laser wavelengths are indicated below each image.

$$E_e = h\nu - (V_{ion} - E_R), \qquad (1)$$

where V_{ion} is the energy of the ionization threshold and E_R the energy of the resonantly excited state. By increasing the laser intensity a Rydberg state can shift into resonance with the n photon dressed ground state, populating this Rydberg state for a specified laser intensity and wavelength. As a

consequence a new ionization channel opens. After the excitation, only one additional photon is needed to finally ionize the atom. Due to the inhomogeneous intensity distribution at the laser focus, both regimes will result in a sharp electron energy distribution, because the shift of the Rydberg state, as well as the ionization potential, are roughly equal and the duration of the laser pulse is short compared to the time the
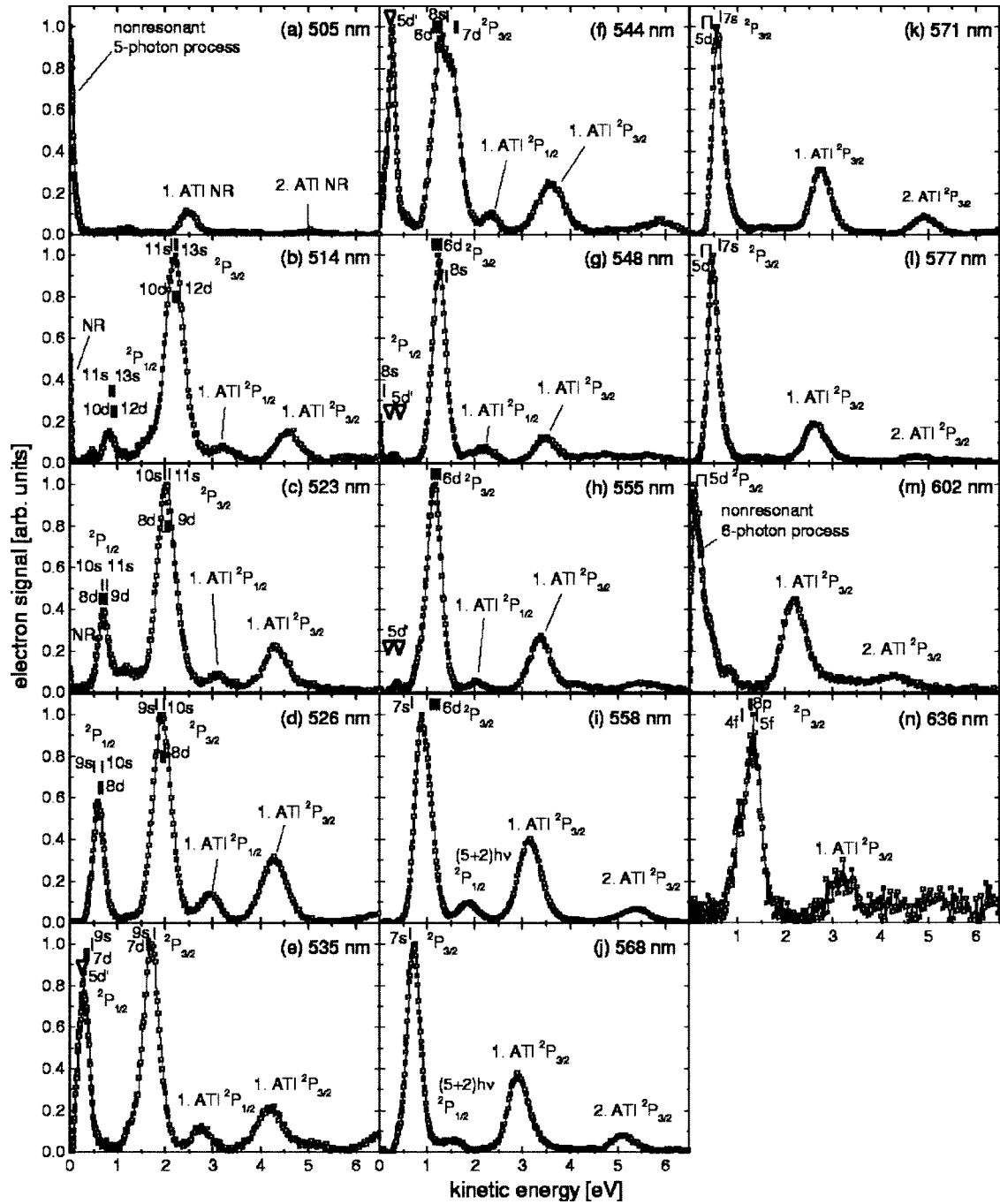
FIG. 3. Polar plots of the electron momentum distribution recorded at different wavelengths and an intensity of 1.3×10^{13} W/cm^2. The laser polarization is directed along the vertical axis of the figure. The laser wavelengths are indicated below each image.

electron requires to leave the focal region. Figure 4 shows the unperturbed energy levels of xenon. The solid curves give the energy of 5, respectively, 6 photons (including the ac Stark shift) and helps to identify the populated Rydberg states for a given wavelength. As an example we show the states accessible at 558 nm. This transition is symbolized by the arrows. For the more detailed discussion of the reso-

nances, that can be excited we use the Racah notation [18] $(^2P^o_{J_c})nl[K]^o_J$. n is the main quantum number, J_c is the angular momentum of the Xe$^+$ ion core, which couples with the orbital angular momentum l of the Rydberg electron giving the quantum number K. The ground state of the xenon ion is always a ^2P state which stands for an angular momentum of 1 and a spin multiplicity of 2. Therefore we have two fine

FIG. 4. Energy level diagram for both fine structure states $^2P_{3/2}$ and $^2P_{1/2}$ of xenon. Only the states that are relevant for the interpretation of the photoelectron spectra are shown. The solid curves represent the energy of 5, respectively, 6 photons in dependence of the wavelength for the two different peak intensities 5×10^{12} W/cm^2 and 1.3×10^{13} W/cm^2, including the ac Stark shift given by Eq. (3). The influence of the temporal and spatial intensity distribution of the laser pulse is demonstrated by the dashed curve. It shows as an example the energy of 5 photons including the ac Stark shift, when the intensity I of the laser is $1/e^2$ of the peak intensity I_1. This leads to contributions from different ionization channels.

FIG. 5. Kinetic energy spectra of the photoelectrons at 5×10^{12} W/cm^2. The wavelength was varied between 505 to 636 nm.

structure states $^2P_{1/2}$ and $^2P_{3/2}$. The coupling of K and the spin of the electron then gives the total angular momentum quantum number J. With a $J_c = 3/2$ core and absorption of an odd number of photons, four different d states namely $(^2P_{3/2}^o)nd[1/2, 3/2]_1^o$ and $(^2P_{3/2}^o)nd[5/2, 7/2]_3^o$ and one s state $(^2P_{3/2}^o)ns[3/2]_1^o$ can be populated. If the angular momentum of the ion core is $1/2$ only the $(^2P_{1/2}^o)nd'[3/2]_1^o$, $(^2P_{1/2}^o)nd'[5/2]_3^o$, and $(^2P_{1/2}^o)ns'[1/2]_1^o$ intermediate states can be reached.

B. Nonresonant ionization

In the nonresonant case we obtain

$$E_e = mh\nu - (V_{ion} + U_P) \qquad (2)$$

for the kinetic energy of photoelectrons. Here m is the number of photons required to ionize a xenon atom and U_P the ponderomotive shift. The shift can be calculated by the equation

$$U_P[\text{eV}] = 9.33 \times 10^{-14} I[\text{W/cm}^2]\lambda^2[\mu\text{m}^2]. \qquad (3)$$

For the peak pulse intensities used in this experiment the maximum shift lies between $0.1-0.4$ eV. According to Eq. (2), electrons born at different laser intensities appear at different photoelectron energies. As a consequence of the inten-
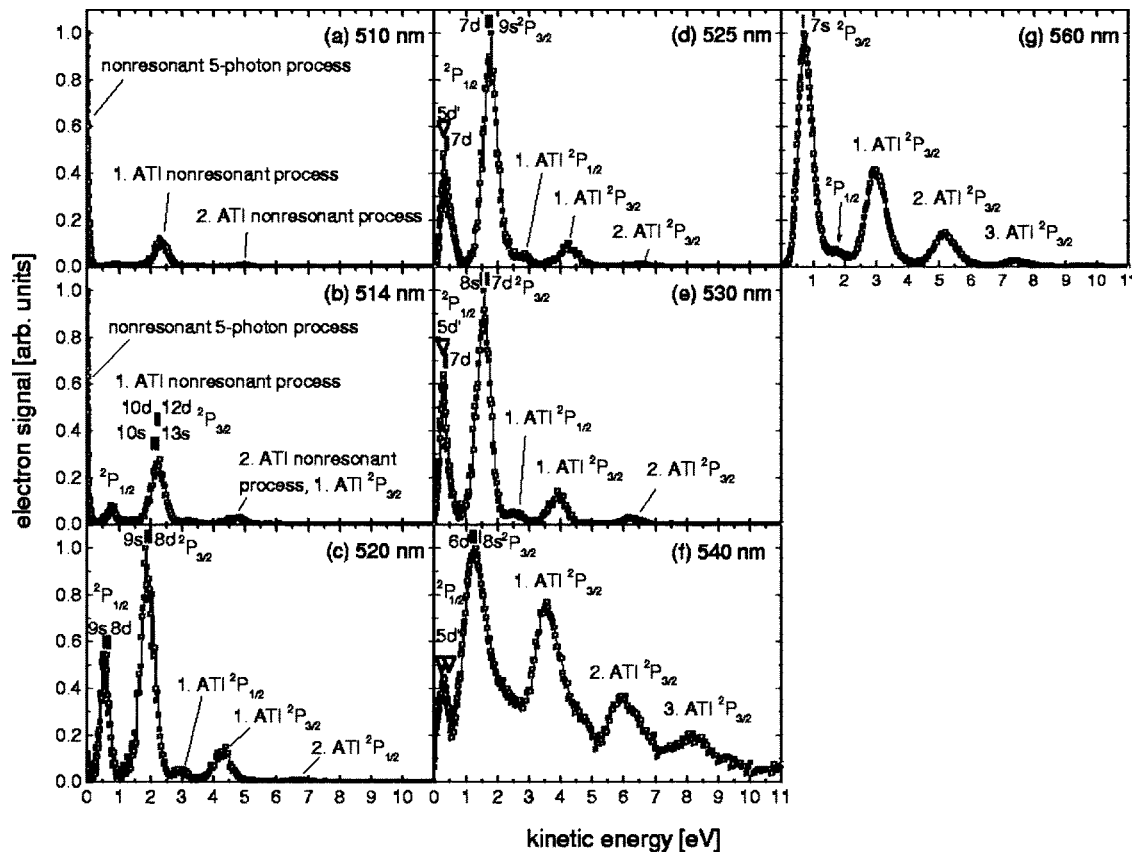
FIG. 6. Photoelectron kinetic energy spectra for wavelengths between 510 to 560 nm and an intensity of 1.3×10^{13} W/cm^2.

sity distribution at the focus we expect a broader electron distribution. This effect is most pronounced at low electron energy. This can be seen, respectively, in Fig. 2 at 505 nm, for the 5-photon, and at 602 and 613 nm, for the 6-photon nonresonant process.

V. DISCUSSION OF RESONANT AND NONRESONANT PROCESSES

The used wavelengths allow the observation of nonresonant ionization (with 5 and 6 photons) as well as resonant (5+1)- and (6+1)-photon ionization processes. Therefore the following chapter is divided in three parts. Experimental results were taken at two different laser intensities, 5×10^{12} and 1.3×10^{13} W/cm^2. Whenever it is necessary the influence of the laser intensity is discussed in the same part.

A. 5- and 6-photon nonresonant ionization

Due to the temporal and spatial intensity distribution in the laser focus, 5-photon nonresonant ionization plays a role at wavelengths which are lower than multiphoton resonances, as seen in the results for 505, 514, and 523 nm, for 5×10^{12} W/cm^2 leading to low kinetic energy electrons (circlelike structures in the center of the images in Fig. 2). At 505 nm also high Rydberg states (with $n \geqslant 12$) can be reached with 5 photons (see Fig. 4), but the nonresonant ionization is the dominant process, because of the broad structureless electron energy distribution, which is typical for

this process [6]. For wavelengths higher than 505 nm lower excited states are shifted into resonance and the photoelectron yield of the nonresonant 5-photon process drops dramatically. Then the resonance enhanced (5+1)-photon ionization plays the leading role. Tuning the system to a higher intensity of 1.3×10^{13} W/cm^2 raises the ponderomotive shift by a factor of 2.6. This means that the nonresonant ionization channel closes at a lower wavelength and therefore we observe nonresonant ionization only at 510 and 514 nm. We cannot see nonresonant 5-photon ionization at 520 nm and higher wavelengths (Fig. 3). The 6-photon nonresonant ionization channel was monitored at 602 nm for 5×10^{12} W/cm^2, leading to 0.12 eV photoelectrons. As shown in Fig. 4 the process overlaps with the (5+1)-photon resonant ionization via $5d$ Rydberg states, so relative broad structures appear in the image and the photoelectron kinetic energy spectra. At 613 nm the signal of the photoelectrons which ionized into this channel is much weaker and at 636 nm the 6-photon nonresonant channel is closed.

B. (5+1)-photon resonant ionization: The Xe$^+$ $^2P_{3/2}$ and $^2P_{1/2}$ channels

Experiments are carried out at two different laser intensities, 5×10^{12} and 1.3×10^{13} W/cm^2.

1. Discussion of the results at 5×10^{12} W/cm^2

In the case of a (5+1)-photon resonant process an excited state of xenon can be reached with 5 photons and ionization

TABLE I. Coefficients of expansion in Legendre polynomials $P_{l,m=0}(\cos(\theta))$ obtained in least-square fits. The intensity of the laser pulse is 5×10^{12} W/cm^2.

	Wavelength (nm)	β_0	β_2	β_4	β_6	β_8	β_{10}
$^2P_{3/2}$	514	1 ± 0.009	1.773 ± 0.019	0.909 ± 0.026	0.369 ± 0.031	-0.462 ± 0.036	0.089 ± 0.041
(5+1) photons	523	1 ± 0.021	1.586 ± 0.041	0.773 ± 0.056	0.479 ± 0.068	-0.373 ± 0.078	
	526	1 ± 0.007	1.370 ± 0.015	0.912 ± 0.020	0.782 ± 0.025	-0.629 ± 0.028	0.151 ± 0.032
	535	1 ± 0.013	1.295 ± 0.025	0.943 ± 0.035	1.368 ± 0.042	-0.377 ± 0.049	0.110 ± 0.055
	544	1 ± 0.014	1.482 ± 0.027	0.807 ± 0.037	0.461 ± 0.045	-0.567 ± 0.052	
	548	1 ± 0.011	1.750 ± 0.023	0.991 ± 0.032	0.607 ± 0.038	-0.140 ± 0.044	0.314 ± 0.050
	555	1 ± 0.011	1.199 ± 0.023	0.607 ± 0.031	0.884 ± 0.038	-0.485 ± 0.043	
	558	1 ± 0.006	1.720 ± 0.013	1.800 ± 0.018	2.150 ± 0.021	-0.230 ± 0.025	-0.037 ± 0.028
	568	1 ± 0.026	1.880 ± 0.052	1.520 ± 0.071	1.390 ± 0.084		
	571	1 ± 0.008	1.590 ± 0.016	1.035 ± 0.022	1.135 ± 0.026		
	577	1 ± 0.008	2.010 ± 0.016	1.300 ± 0.022	0.824 ± 0.026	-0.071 ± 0.031	0.071 ± 0.034
$^2P_{1/2}$	514	1 ± 0.033	1.448 ± 0.067	0.664 ± 0.091	0.663 ± 0.111	0.531 ± 0.127	
(5+1) photons	523	1 ± 0.021	1.640 ± 0.041	1.201 ± 0.057	0.830 ± 0.069	0.083 ± 0.080	0.199 ± 0.090
	526	1 ± 0.010	1.910 ± 0.021	1.164 ± 0.029	0.540 ± 0.034		
	535	1 ± 0.015	2.230 ± 0.031	1.770 ± 0.042	0.910 ± 0.051	-0.110 ± 0.059	0.243 ± 0.066
	544	1 ± 0.013	2.280 ± 0.027	2.100 ± 0.037	1.590 ± 0.045	-0.092 ± 0.051	

occurs after the absorption of an additional photon. The kinetic energy of the corresponding photoelectron can be calculated with Eq. (1). We start with the analysis for the images recorded at 5×10^{12} W/cm^2 (see Fig. 2). At 505 nm, besides the bright circle in the center of the image due to 5-photon nonresonant ionization of xenon atoms, two concentric rings appear that can be interpreted as ATI. Tuning the NOPA system to a wavelength of 514 nm turns excited levels into 5-photon resonance and additional rings appear in the images. The ring at 2.2 eV belongs to electrons ionizing into the $^2P_{3/2}$ channel and the ring at 0.8 eV to ionization into the $^2P_{1/2}$ channel. The two outer rings at 3.2 eV and 4.6 eV are the first ATI orders of both fine structure channels. For higher wavelengths lower excited states are shifted into resonance, which leads to electrons with less kinetic energy

and therefore the radii of the rings decrease. The $^2P_{1/2}$ ionization channel closes for wavelengths greater than 548 nm, but structures of the (5+2) resonant MPI process into this channel can still be seen in the spectra up to a wavelength of 568 nm. Finally at 636 nm resonant (6+1)-photon processes via p- and f-character Rydberg states occur. More detailed information about the intermediate resonant states of xenon can be gathered through an analysis of the photoelectron kinetic energy spectra given in Fig. 5 For a better orientation the expected peak positions calculated with Eq. (1), assuming a resonant $(n+1)$ MPI process, are also shown in the spectra. The upper marks belong to ionization into the $^2P_{3/2}$ and the lower marks to the $^2P_{1/2}$ channel. At 505 nm [Fig. 5(a)] the main process is 5-photon nonresonant ionization into the $^2P_{3/2}$ channel. For higher wavelengths excited states

TABLE II. β parameters of the expansion in Legendre polynomials $P_{l,m=0}(\cos(\theta))$ obtained in least-square fits (pulse peak intensity, 1.3×10^{13} W/cm^2).

	Wavelength (nm)	β_0	β_2	β_4	β_6	β_8	β_{10}
$^2P_{3/2}$	514	1 ± 0.012	2.330 ± 0.024	1.740 ± 0.033	0.827 ± 0.040	-0.110 ± 0.047	0.132 ± 0.052
(5+1) photons	520	1 ± 0.020	2.490 ± 0.040	2.260 ± 0.060	1.480 ± 0.070	-0.090 ± 0.080	
	525	1 ± 0.019	2.110 ± 0.038	1.920 ± 0.053	2.260 ± 0.064	0.124 ± 0.074	0.132 ± 0.083
	530	1 ± 0.028	2.010 ± 0.057	1.800 ± 0.078	2.040 ± 0.093		
	540	1 ± 0.014	1.630 ± 0.028	1.315 ± 0.038	1.246 ± 0.046	-0.690 ± 0.054	0.140 ± 0.060
	560	1 ± 0.006	2.050 ± 0.011	1.540 ± 0.015	1.330 ± 0.019	-0.057 ± 0.022	0.091 ± 0.024
$^2P_{1/2}$	514	1 ± 0.040	1.800 ± 0.090	1.160 ± 0.120	0.980 ± 0.140		
(5+1) photons	520	1 ± 0.060	2.400 ± 0.110	2.000 ± 0.160	1.200 ± 0.190	0.510 ± 0.220	
	525	1 ± 0.041	2.690 ± 0.082	1.900 ± 0.113	0.770 ± 0.137	0.584 ± 0.159	0.429 ± 0.178
	530	1 ± 0.025	2.300 ± 0.051	2.010 ± 0.070	1.490 ± 0.085	0.710 ± 0.099	0.660 ± 0.110
	540	1 ± 0.060	1.890 ± 0.110	1.930 ± 0.150	0.740 ± 0.180		

are shifted into resonance and (5+1)-photon resonant processes into both ionic fine structure states can be observed. The closing of the $^2P_{1/2}$ channel can clearly be seen in the difference of the spectra between 535 and 555 nm [Figs. 5(e)–5(h)]: The main peak in the 535 nm spectrum at 1.7 eV can be explained with intermediate 7*d* and 9*s* excited Rydberg states and ionization into the $^2P_{3/2}$ channel. Resonance structures can also be found at 0.43 eV due to ionization into the $^2P_{1/2}$ channel. At 544 nm the 6*d*, 8*s*, and 7*d* Rydberg states are shifted into resonance and peak structures are found between 1.1 to 1.7 eV in the kinetic energy spectrum. Ionization of the 6*d* Rydberg state into the $^2P_{1/2}$ fine structure state closes at this wavelength, but strong structures belonging to this channel can still be found at 0.3 eV. Tuning the system to 548 nm mainly shifts the 6*d* states into resonance. The small peak at lower kinetic energy can be interpreted with a contribution of 8*s*- and 5*d'*-resonant states ionizing into the $^2P_{1/2}$ channel. Broad structures appear at 602 nm [Fig. 5(m)] in the energy interval [0 eV, 1 eV]. They can be explained with 5*d* resonances overlapping with the 6-photon nonresonant process. At 636 nm the (5+1)-photon resonant processes vanishes, because 7 photons of this wavelength are needed to ionize xenon.

2. Discussion of the results at an intensity of 1.3×10^{13} W/cm²

The discussion for the data recorded at 1.3×10^{13} W/cm² is similar. We have the bright circles in the middle of the images in Fig. 3 at 510–520 nm due to 5-photon nonresonant ionization. The two inner rings corresponding to the two fine structure ionization channels and the outer rings to their first ATI orders. The expected photoelectron kinetic energy spectra are shown in Fig. 6. The closing of the $^2P_{1/2}$ channel occurs between 540 and 560 nm, but like in Fig. 5 structures from the (5+2)-resonant process into this channel are still visible at the higher wavelength of 560 nm.

3. Contribution of the 5*d'* states

Another interesting aspect are the contributions of the $5d'[3/2]_1^o$ and $5d'[5/2]_3^o$ resonant states, that should be observed in the intensity and wavelength region we covered in our experiments. Energetically the $5d'[3/2]_1^o$ level lies between the 7*d* and 8*d* states and the $5d'[5/2]_3^o$ below the 7*d* states (cf. Fig. 4). Rottke *et al.* [9] monitored sharp resonance structures of these states at 526.5 nm. They found the $5d'[3/2]_1^o$ resonance at an intensity of 2.5×10^{13} W/cm² and the $5d'[5/2]_3^o$ at 3.5×10^{13} W/cm². This is in good agreement with our observations. We find very narrow peak structures at 535 and 544 nm for 5×10^{12} W/cm² [Figs. 5(e) and 5(f)], and at 525 and 530 nm for 1.3×10^{13} W/cm² [Figs. 6(d) and 6(e)] due to a $5d'[5/2]_3^o$ resonance. The expected peak positions of the 5*d'* states are marked with triangles. We can also confirm the observation [9] that the probability of ionization of these states into the $^2P_{3/2}$ ionic state is low, because we did not observe a contribution of these states into this fine structure channel.
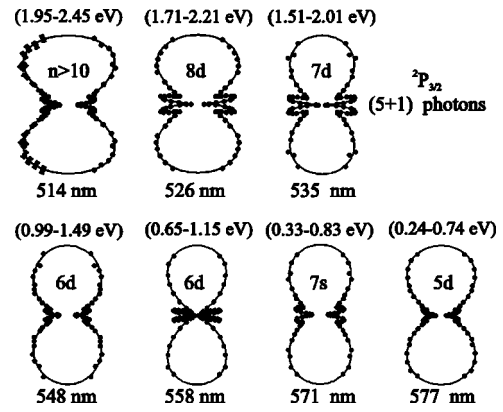

FIG. 7. Polar plots of the angular distributions within the energy range indicated in parantheses recorded at 5×10^{12} for the (5+1)-photon resonant ionization into the $^2P_{3/2}$ channel. The circles represent the experimental data and the solid lines the fit with a superposition of Legendre polynomials.

C. (6+1)-photon resonant ionization

Images of the (6+1)-photon resonant process were recorded at 636 nm and 5×10^{12} W/cm² peak pulse intensity. The image is shown in Fig. 2 and the photoelectron kinetic energy spectrum in Fig. 5(n). With the same arguments given in the discussion of the (5+1)-resonant ionization, the following *p* and *f* Rydberg states with a $^2P_{3/2}^o$ ion core can be excited with 6 photons: $(^2P_{3/2}^o)np[3/2,5/2]_2$, $(^2P_{3/2}^o)np[1/2^o]_0$, $(^2P_{3/2}^o)nf[3/2,5/2]_2$, $(^2P_{3/2}^o)nf[7/2,9/2]_4$. In the same way the $2P_{1/2}^o$ ionic ground state, the $(^2P_{1/2}^o)np'[3/2^o]_2$ and $(^2P_{1/2}^o)np'[1/2]_0$ levels, can be reached. We do not observe *f* Rydberg states with a $^2P_{1/2}$ fine structure core because of their autoionizing character. We could monitor resonance structures due to contributions of 4*f*, 8*p*, and 5*f* intermediate Rydberg states.

VI. ANGULAR DISTRIBUTIONS

To obtain the information about the angular distributions we integrate the concentric rings of the Abelian transformed CCD images over a radius interval $[r-dr, r+dr]$ ($dr = 250$ meV) for the radius and for angles taken between 0° and 180° in steps of 4°. Fits of the data were performed with a superposition of Legendre polynomials

$$I(\theta) = \sum_{k=0}^{n} \beta_{2k} P_{2k,m=0}(\cos(\theta)), \qquad (4)$$

where θ is the angle between the laser polarization axis and the electron emission. The fits include only data for $\theta \in [10°, 170°]$, because the Abelian transformation produces noise along the laser polarization axis, i.e., around 0 and 180 degrees. The β parameters for 5×10^{12} W/cm² are given in Table I and for 1.3×10^{13} W/cm² in Table II. Polar plots for some of the angular distributions are shown in Fig. 7. The plots reveal, that the angular momentum quantum number of the resonant state has a great influence on the angular distribution. If a *d* state is shifted into resonance, the

f character of the distribution of the photoelectrons is increased, i.e., transitions with $\Delta l = 1$ are preferred.

VII. CONCLUSIONS

We have observed MPI of xenon atoms with femtosecond laser pulses. Besides nonresonant processes we found resonance structures in both $^2P_{3/2}$ and $^2P_{1/2}$ fine structure channels. Between 505 and 602 nm the resonant states could be identified as s- and d-angular momentum states. At 636 nm p- and f-momentum states were shifted into resonance. In the wavelength region we covered in our experiments (505–636 nm), ionization into the $^2P_{3/2}$ channel was the dominant process, except if a $5d'$ state was shifted into resonance. In this case the signal of the photoelectrons ionizing into the $^2P_{1/2}$ channel was strongly increased.

[1] P. Agostini, P. Breger, A. L'Huillier, H. Muller, and G. Petite, Phys. Rev. Lett. **63**, 2208 (1989).

[2] R. Vrijen, J. Hoogenraad, H. Muller, and L. Noordam, Phys. Rev. Lett. **70**, 3016 (1993).

[3] E. Mevel, P. Breger, R. Trainham, G. Petite, P. Agostini, A. Migus, J.-P. Chambaret, and A. Antonetti, Phys. Rev. Lett. **70**, 406 (1993).

[4] C. Bordas, M. Dyer, T. Fairfield, H. Helm, and K. Kulander, Phys. Rev. A **51**, 3726 (1995).

[5] V. Shyja, T. Lang, and H. Helm, Phys. Rev. A **57**, 3692 (1998).

[6] R. Wiehle and B. Witzel, Phys. Rev. Lett. **89**, 223002 (2002).

[7] K. Aron and P. Johnson, J. Chem. Phys. **67**, 5099 (1977).

[8] P. Agostini, F. Fabre, G. Mainfray, G. Petite, and N. Rahman, Phys. Rev. Lett. **42**, 1127 (1979).

[9] R. Freeman, P. Bucksbaum, H. Milchberg, S. Darack, D. Schumacher, and M. Geusic, Phys. Rev. Lett. **59**, 1092 (1987).

[10] M. Saeed and H. Helm, Chem. Phys. **179**, 115 (1994).

[11] H. Rottke, J. Ludwig, and W. Sandner, J. Phys. B **29**, 1479 (1996).

[12] M. de Boer and H. Muller, J. Phys. B **27**, 721 (1994).

[13] H. Helm, N. Bjerre, M. Dyer, D. Huestis, and M. Saeed, Phys. Rev. Lett. **70**, 3221 (1993).

[14] T. Wilhelm, J. Piel, and E. Riedle, Opt. Lett. **22**, 1494 (1997).

[15] G. Cerullo, M. Nisoli, and S. de Silvestri, Appl. Phys. Lett. **71**, 3616 (1997).

[16] J. Piel, M. Beutter, and R. Riedle, Opt. Lett. **25**, 180 (2000).

[17] C. Bordas, F. Paulig, H. Helm, and D. Huestis, Rev. Sci. Instrum. **67**, 2257 (1996).

[18] G. Racah, Phys. Rev. **61**, 537 (1942).